# Supplementary Information: Toward a BT.2020 green emitter through a combined multiple resonance effect and multi-lock strategy

Junyuan Liu[1], Yunhui Zhu[2]*, Taiju Tsuboi[1], Chao Deng[2], Weiwei Lou[2], Dan Wang[1], Tiangeng Liu[1], Qisheng Zhang[1,3]*

[1] MOE Key Laboratory of Macromolecular Synthesis and Functionalization, Department of Polymer Science and Engineering, Zhejiang University, Hangzhou 310027, P.R. China.

[2] Zhejiang Hongwu Technology Co., Ltd., Taizhou 317100, P.R. China.

[3] State Key Laboratory of Clean Energy Utilization, Zhejiang University, Hangzhou 310027, P.R. China.

Email: zhuyunhui@hwoled.com, qishengzhang@zju.edu.cn

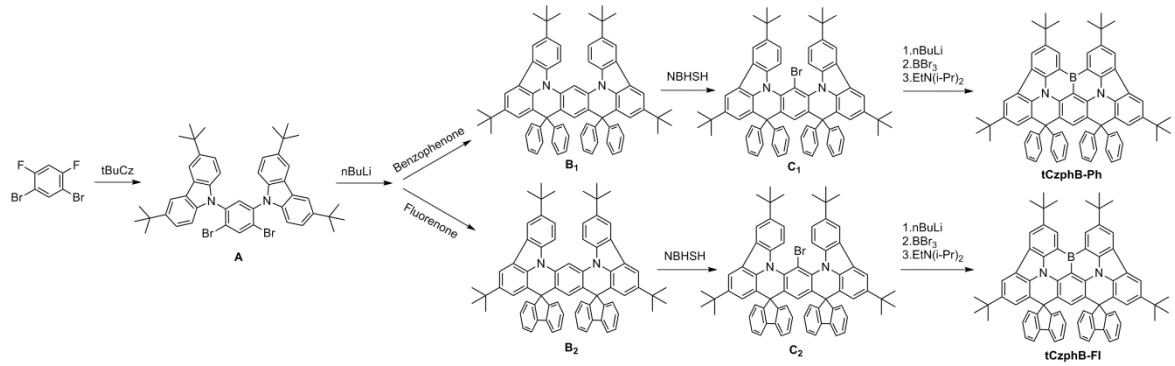


**Supplementary Fig. 1** Synthetic route of tCzphB-Ph and tCzphB-Fl

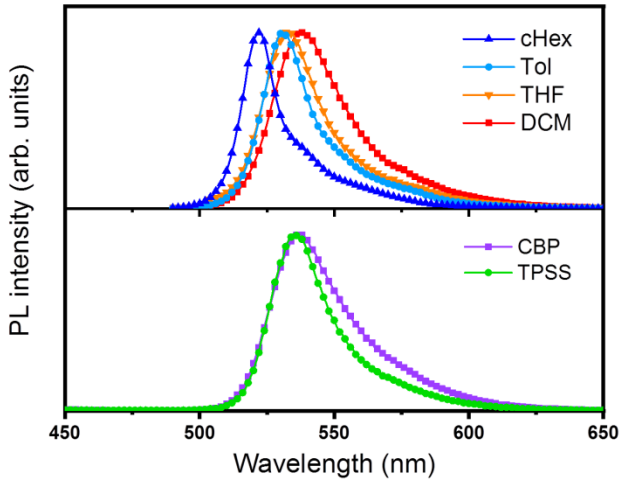


**Supplementary Fig. 2** Normalized fluorescence spectra of tCzphB-Fl in different solutions (cyclohexane, toluene, tetrahydrofuran and dichloromethane) of $1\times10^{-5}$ M and with CBP and TPSS as host at room temperature (RT).

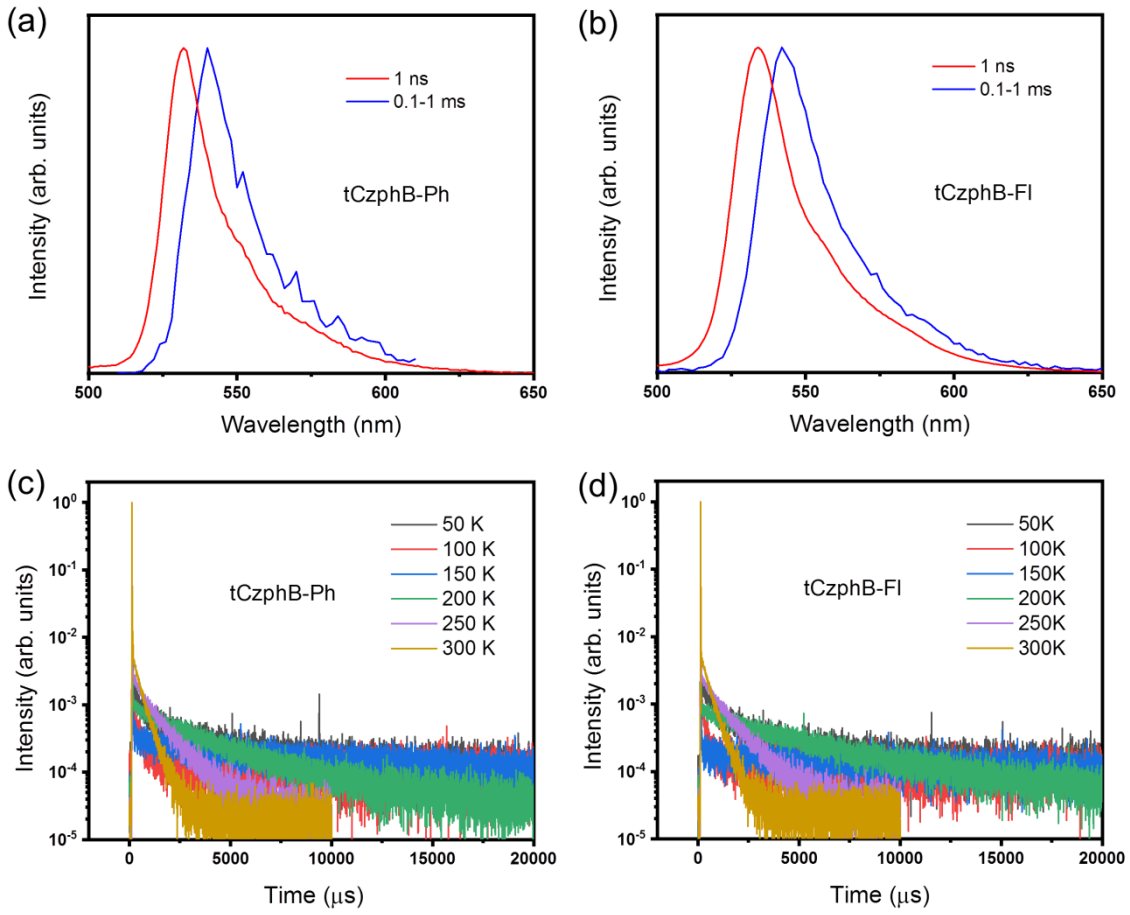


**Supplementary Fig. 3 Emission and transient decay spectra.** Fluorescence (1 ns component) and phosphorescence (0.2−1 ms component) spectra of tCzphB-Ph (**a**) and tCzphB-Fl (**b**) doped into the TPSS films (2 wt%) at 50 K. Transient PL decay spectra of tCzphB-Ph (**c**) and tCzphB-Fl (**d**) doped into the TPSS films (2 wt%) at 50−300 K.

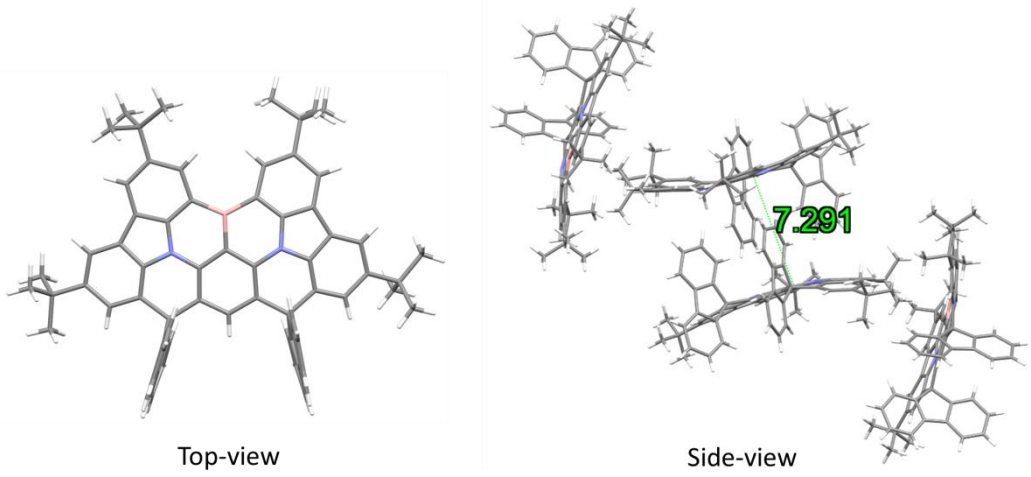


**Supplementary Fig. 4** Crystal structure of tCzphB-Fl from top-view and side-view.

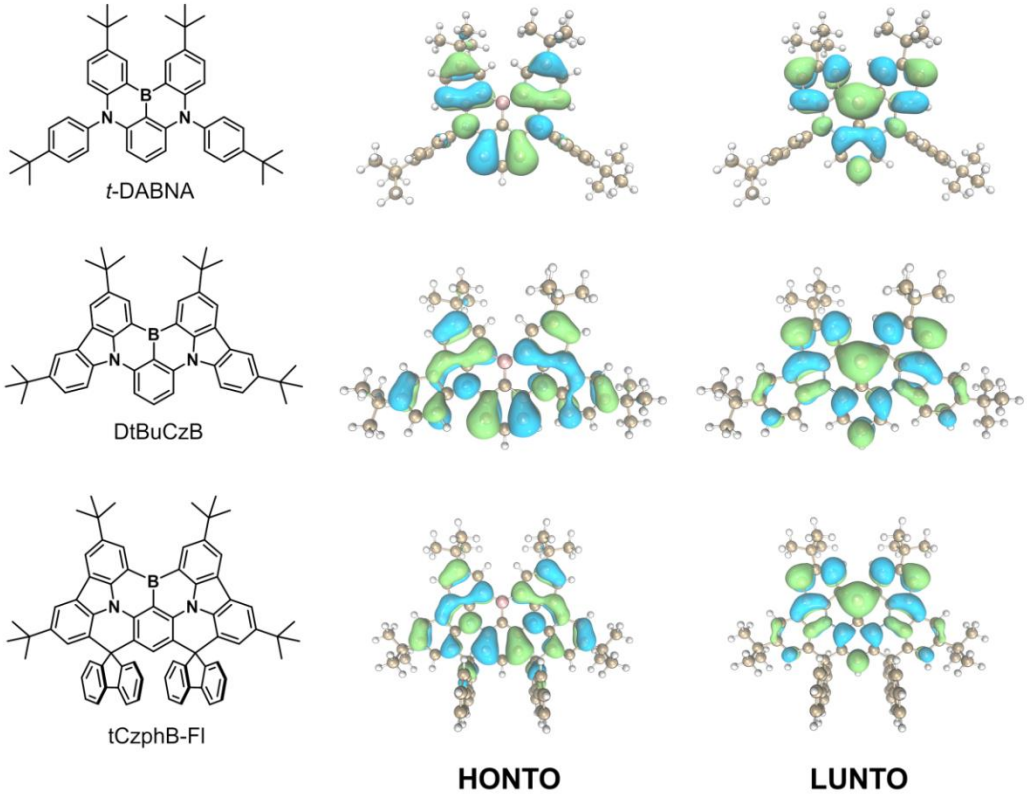


**Supplementary Fig. 5** The natural transition orbitals of $S_1 \rightarrow S_0$ transition of *t*-DABNA, DtBuCzB and tCzphB-Fl. The orbital iso-surface distribution plots at their $S_1$ states calculated at the PBE0/6−31G (d, p) level.

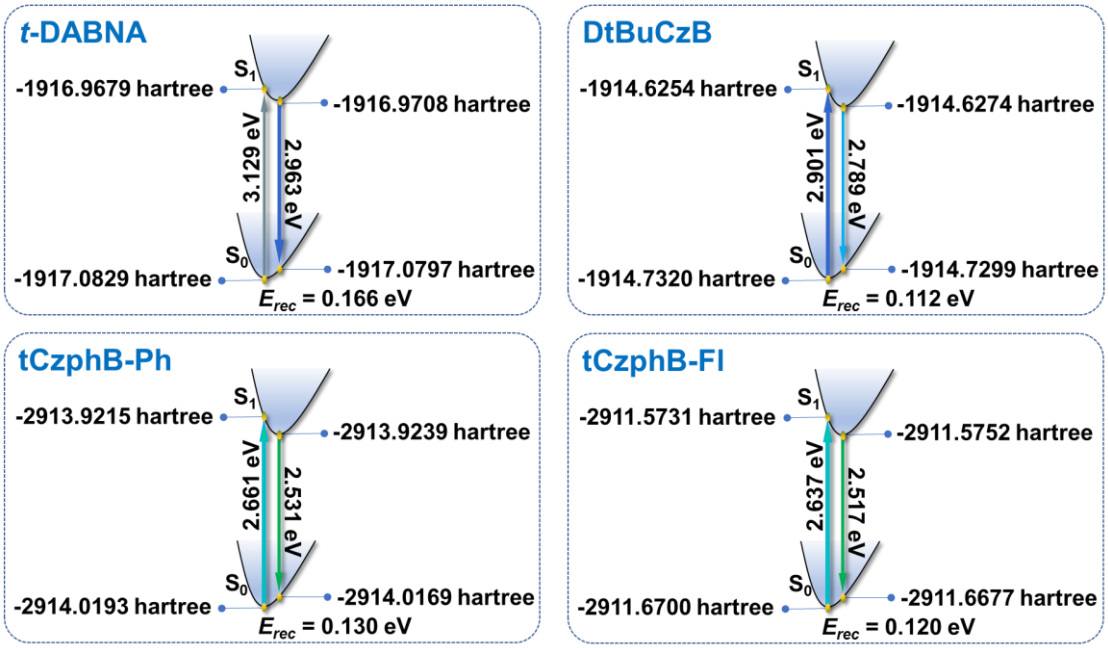


**Supplementary Fig. 6** Potential energy surfaces in the ground and excited states. The transition and reorganization energies were calculated by TD-DFT at the PBE0/6-31G (d, p) level in toluene.

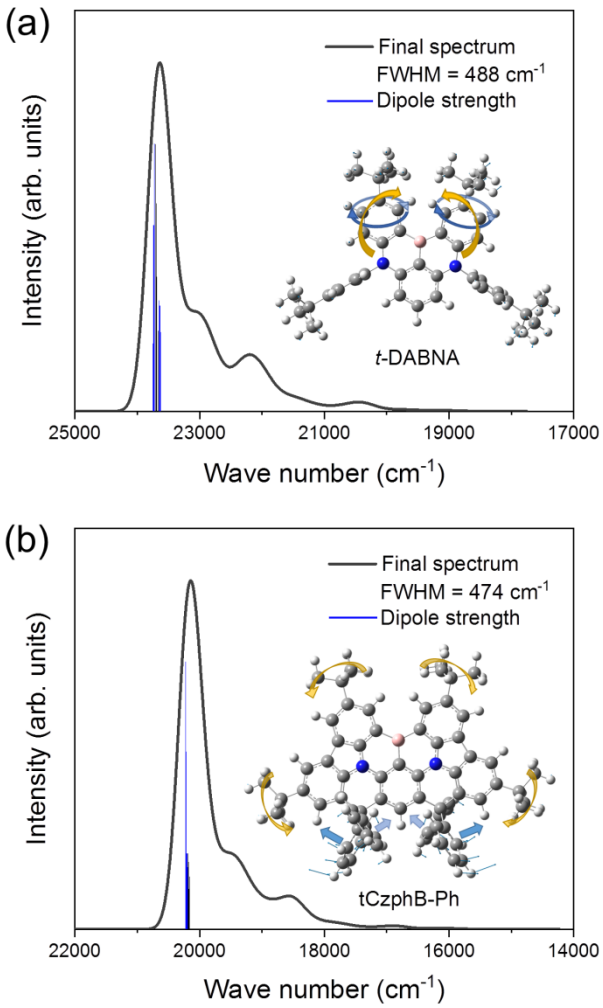


**Supplementary Fig. 7 Spectral simulation.** Simulated vibrationally-resolved fluorescence spectra with dipole strengths of different vibrational modes for **a** *t*-DABNA and **b** tCzphB-Ph.

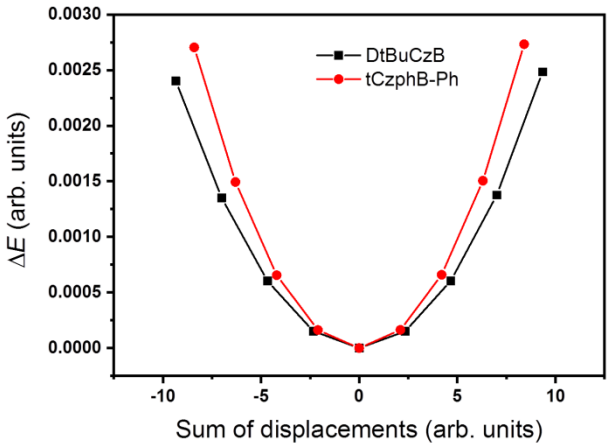


**Supplementary Fig. 8** Vibrational potential energy curves of DtBuCzB and tCzphB-Ph on the basis of their major vibrational mode. Comparing the deformed geometric structures with the ground-state structure in Cartesian coordinates, the sum-modulus-difference for all atoms is recorded as a relative displacement.

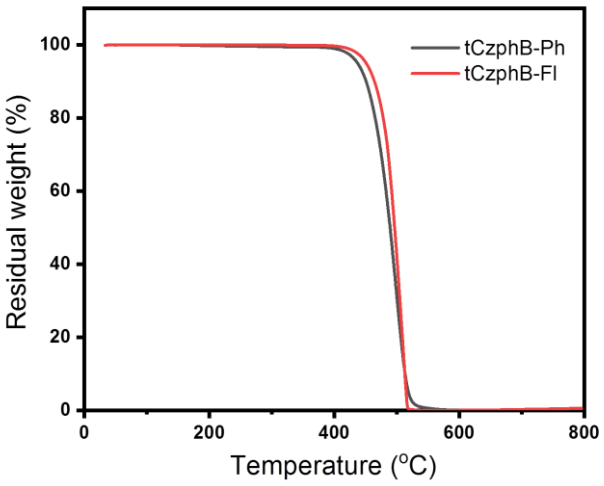


**Supplementary Fig. 9** TGA Curves of investigated compounds under nitrogen flow. The 5 wt% weight-loss-temperatures for tCzphB-Ph and tCzphB-Fl are 437 ℃ and 450 ℃, respectively.

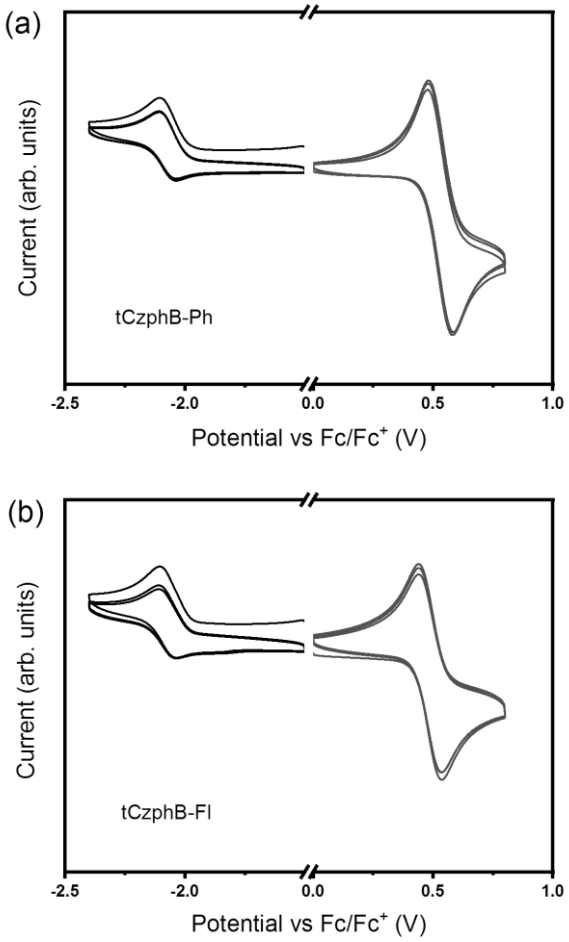


**Supplementary Fig. 10 Cyclic voltammetry measurements.** Cyclic voltammograms of **a** tCzphB-Ph and **b** tCzphB-Fl in DCM (oxidation) and DMF (reduction). The LUMO and HOMO energy level can be obtained from the reduction and oxidation curves following the formula: HOMO = -[$E_{ox}$-$E$(Fc/Fc$^+$) + 4.8] eV and LUMO = -[$E_{re}$ – $E$(Fc/Fc$^+$) + 4.8] eV, respectively.

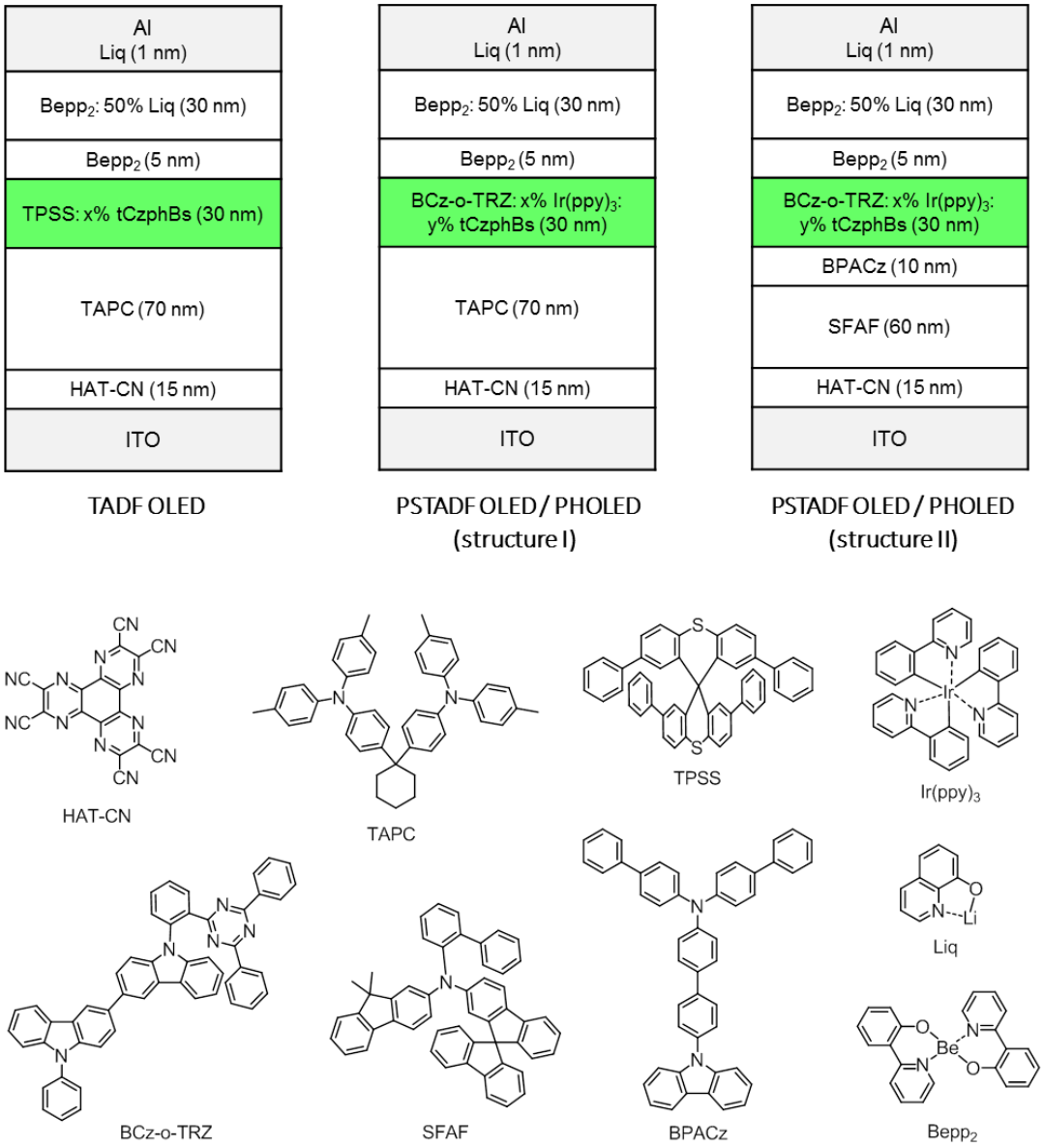


**Supplementary Fig. 11** Structures of the investigated OLEDs and the molecular structures of the materials used in them.

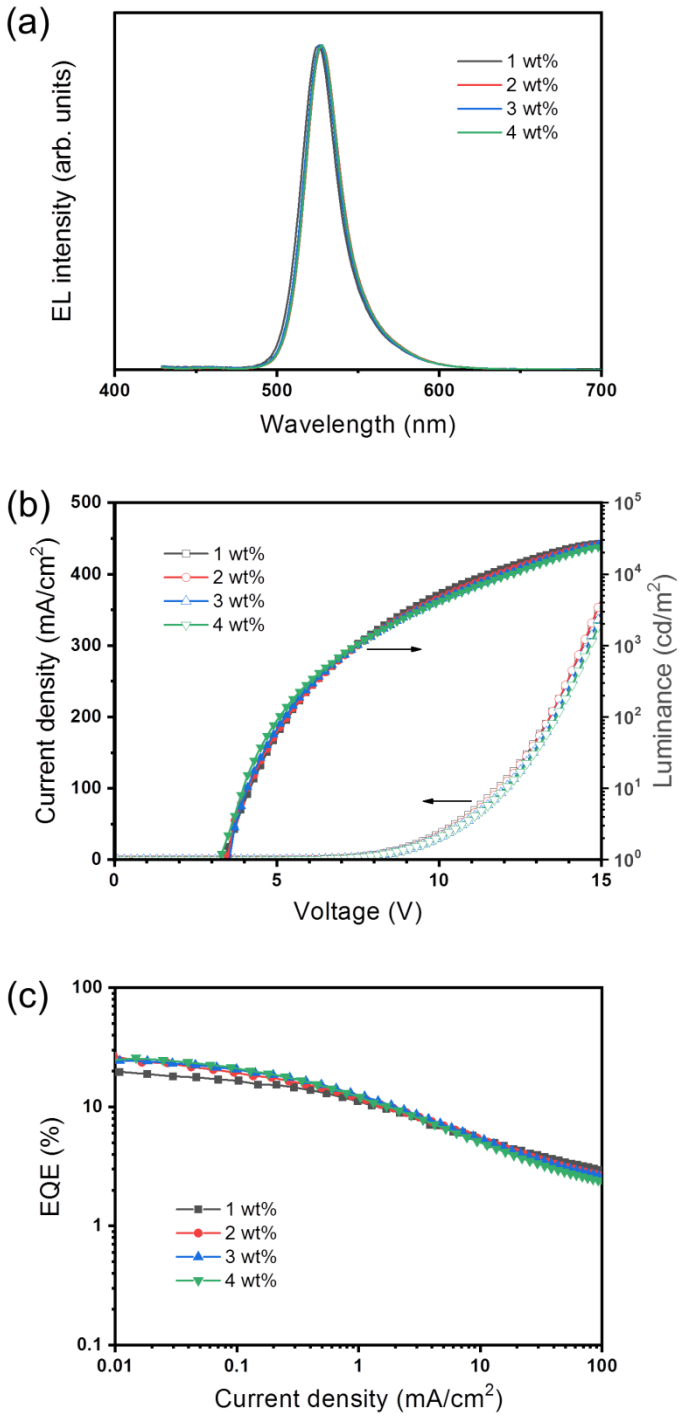


**Supplementary Fig. 12 OLED characteristics.** Electroluminescence spectra at 10 mA/cm$^2$ (**a**), current density–voltage–luminance characteristics (**b**) and EQE–current density characteristics (**c**) of the TADF OLEDs with different concentrations of tCzphB-Ph in TPSS.

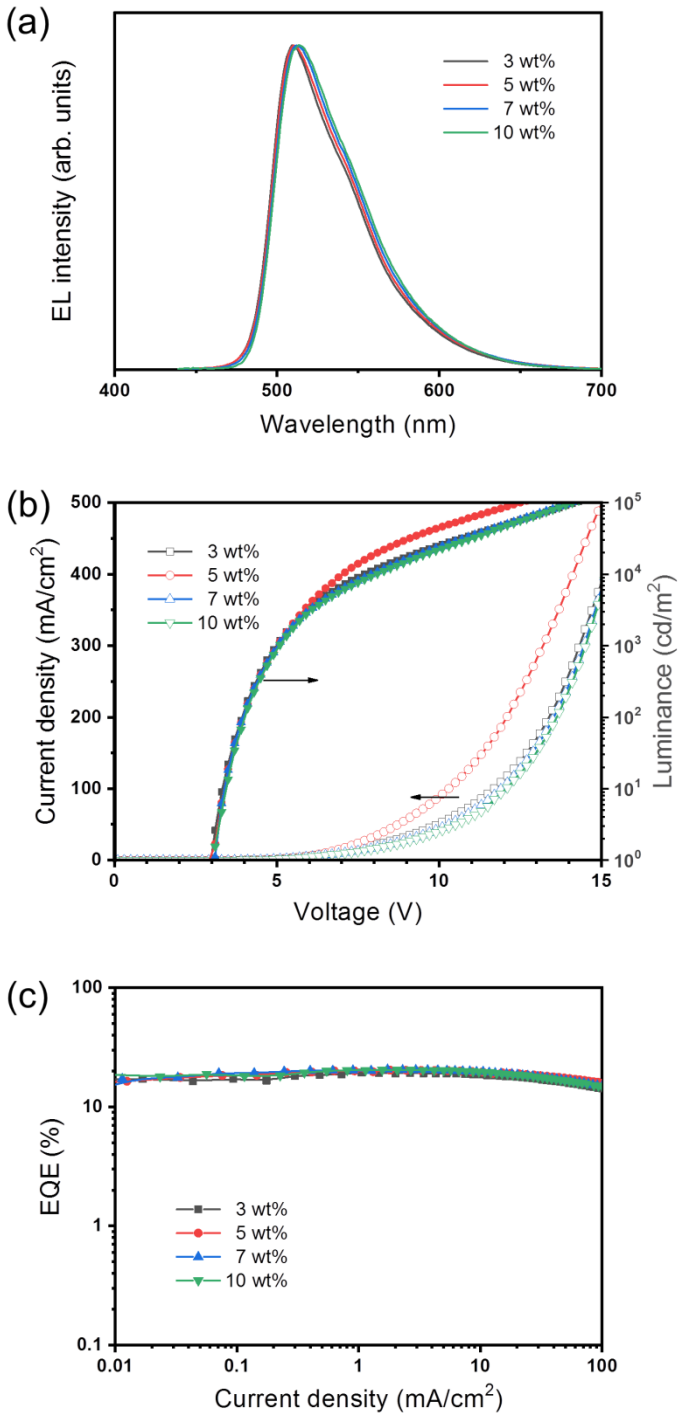


**Supplementary Fig. 13 OLED characteristics.** Electroluminescence spectra at 10 mA/cm$^2$ (**a**), current density–voltage–luminance characteristics (**b**) and EQE–current density characteristics (**c**) of the PHOLEDs with different concentrations of Ir(ppy)$_3$ in BCz-o-TRZ.

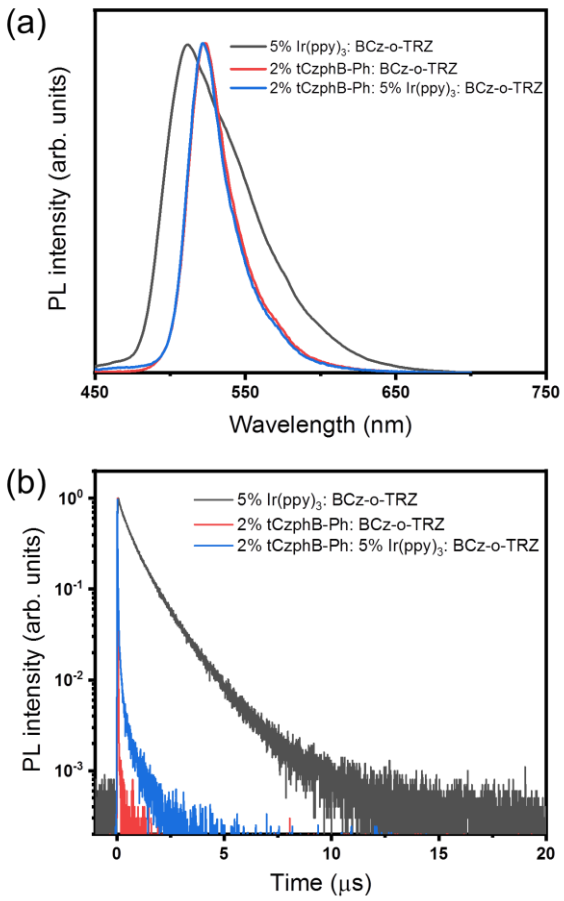


**Supplementary Fig. 14 Steady-state and transient emission.** Emission (**a**) and transient decay (**b**) spectra from the BCz-o-TRZ films doped with 5 wt% $Ir(ppy)_3$, 2 wt% tCzphB-Ph, and both at RT. The wavelength of the excitation light was 370 nm. The PLQY of the double-doped film (0.97) is considerably higher than that of the $Ir(ppy)_3$-single-doped film (0.67) owing to the very efficient Förster resonance energy transfer from $Ir(ppy)_3$ to tCzphB-Ph.

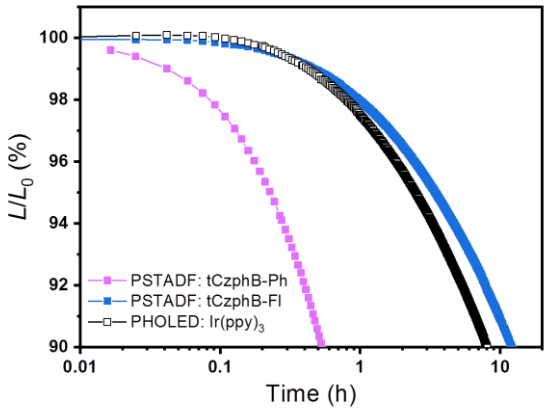


**Supplementary Fig. 15** Relative luminance–operating time characteristics of the PSTADFs and PHOLED (structure I) at a fixed current density of 20 mA/cm$^2$. The initial luminance was $2.33\times10^4$, $2.45\times10^4$, and $1.19\times10^4$ cd/m$^2$ for the devices doping tCzphB-Ph, tCzphB-Fl, and only $Ir(ppy)_3$, respectively.

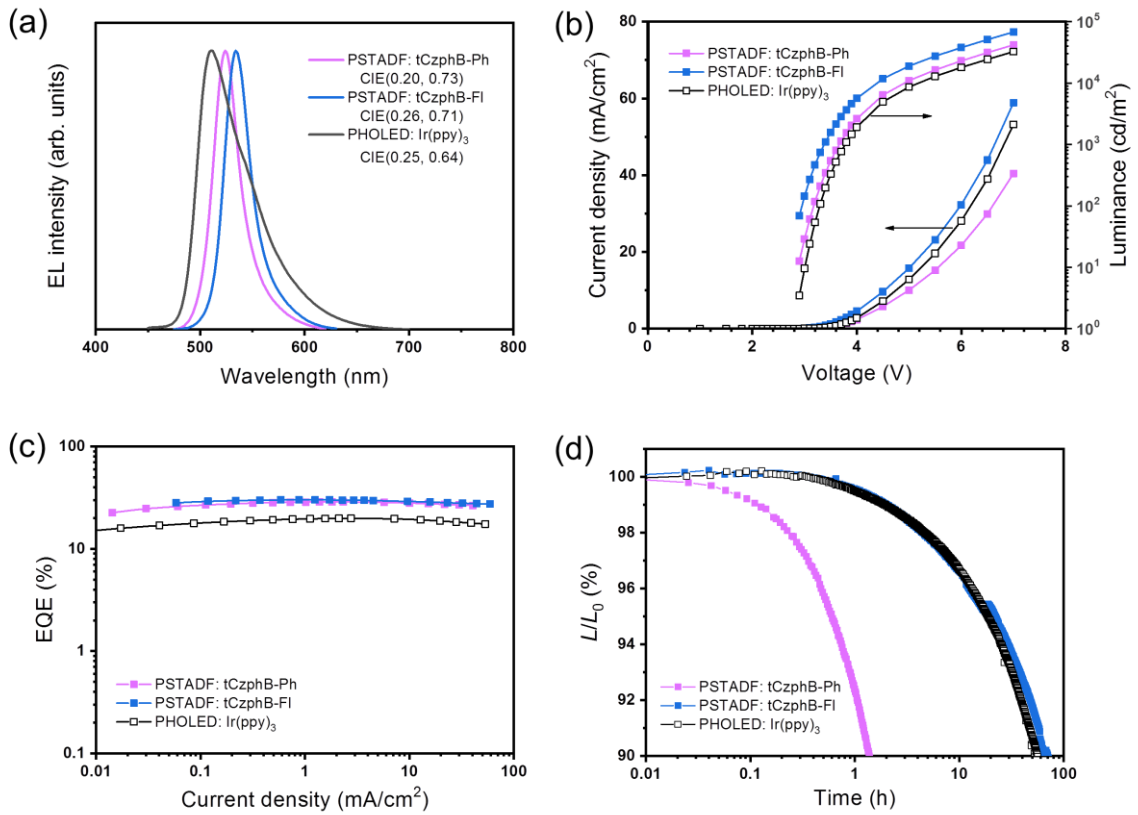


**Supplementary Fig. 16 Performance of the PSTADFs and PHOLED with structure II. a** EL spectra at 20 mA/cm$^2$. **b** Luminance–current density–voltage characteristics. **C** EQE–current density characteristics. **d** Relative luminance–operating time characteristics at a fixed current density of 20 mA/cm$^2$. The initial luminance was $2.14\times10^4$, $2.40\times10^4$, and $1.29\times10^4$ cd/m$^2$ for the devices doping tCzphB-Ph, tCzphB-Fl, and only $Ir(ppy)_3$, respectively.

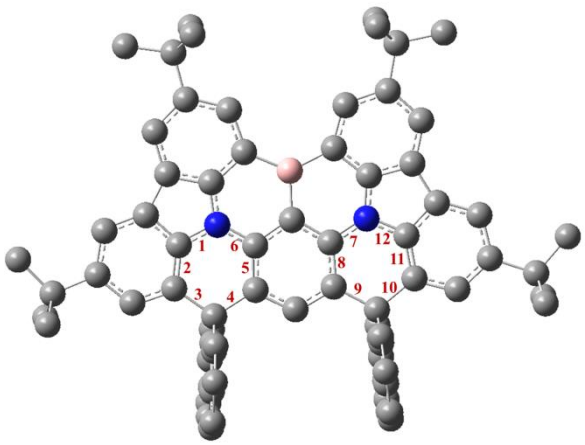


**Supplementary Fig. 17** Number of the selected bonds in the tCzphBs.

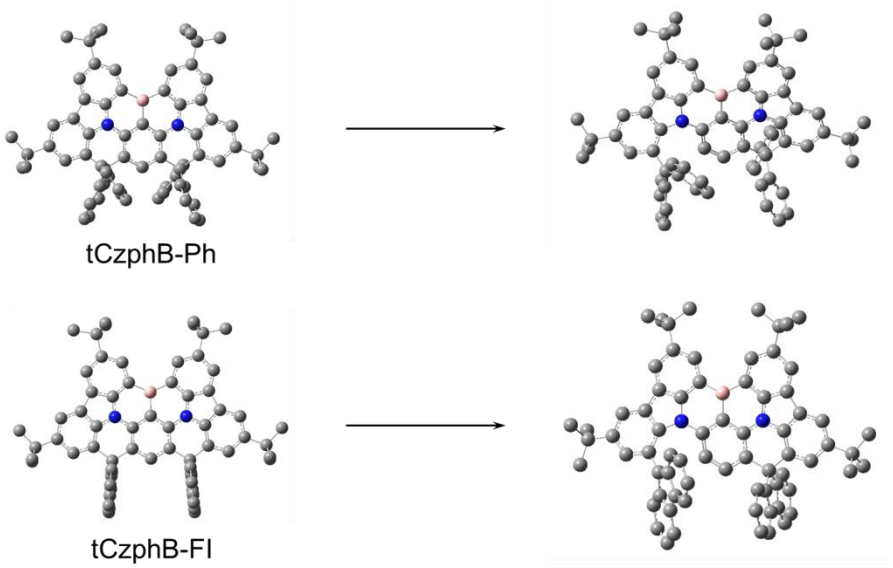


**Supplementary Fig. 18** Homolytic C−C bond dissociation in tCzphBs in their ground states. The bond dissociation energies were calculated to be 4.50 eV for tCzphB-Ph and 4.63 eV for tCzphB-Fl.

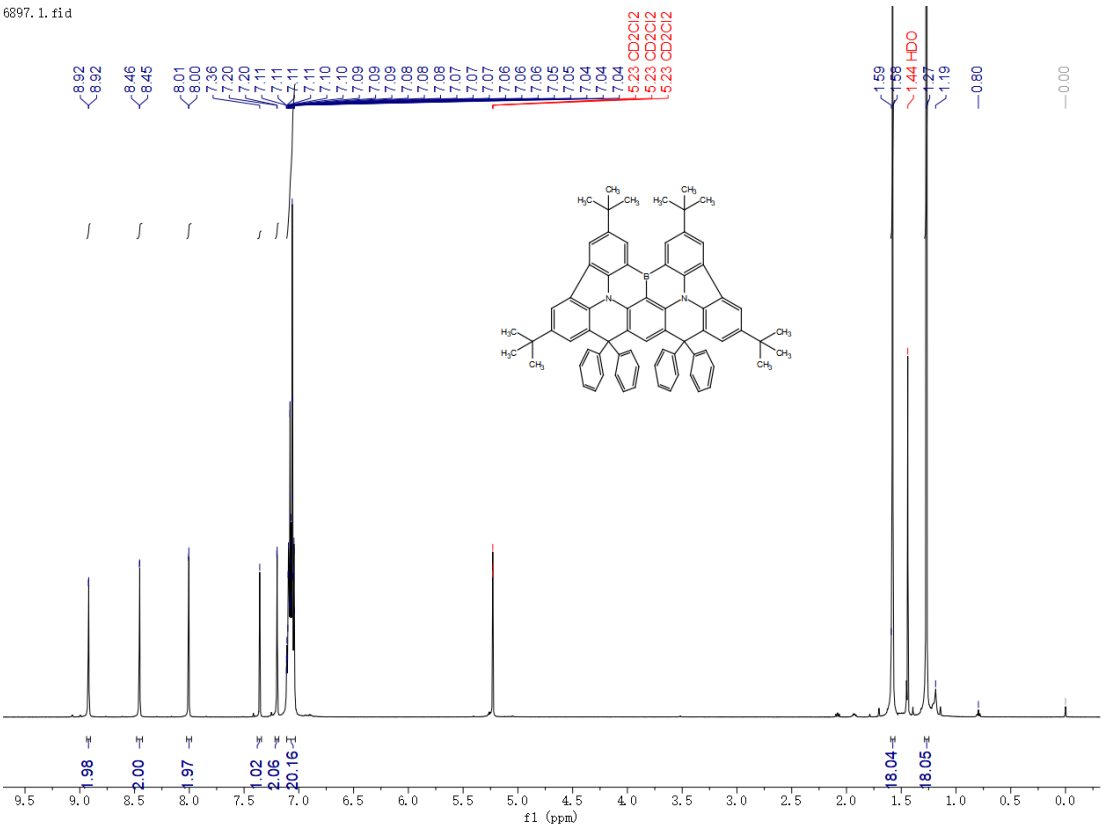


**Supplementary Fig. 19** $^{1}$H NMR spectrum of tCzphB-Ph in $CD_2Cl_2$.

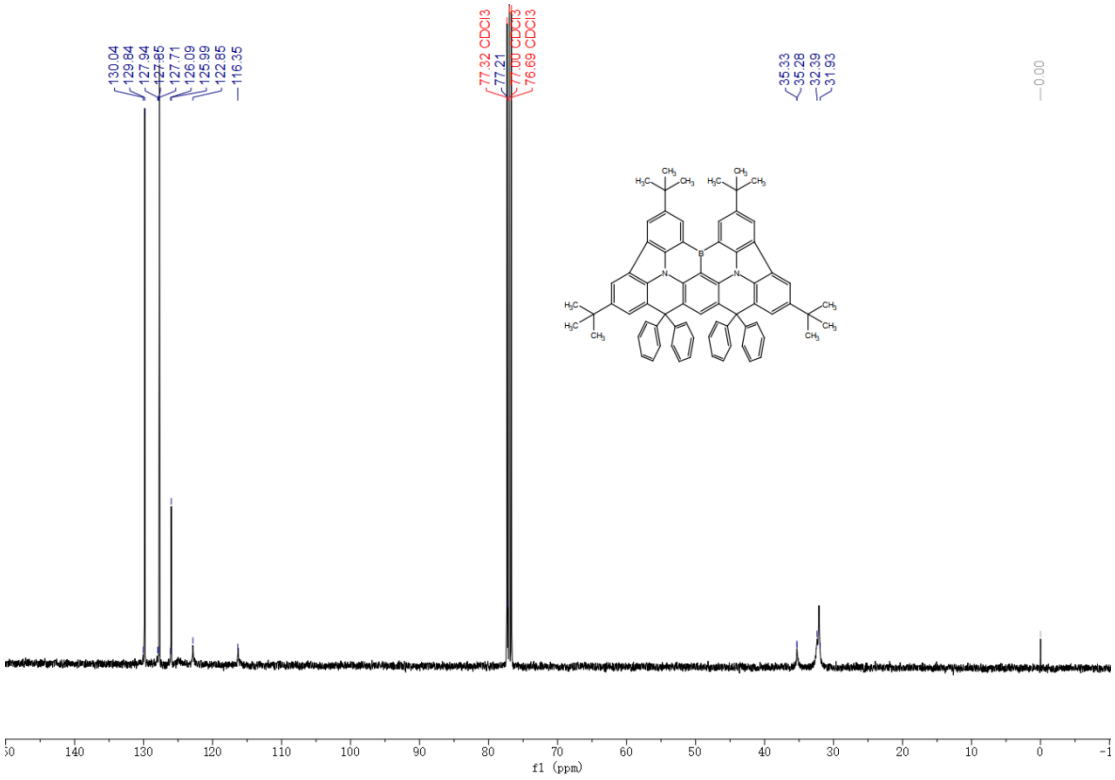


**Supplementary Fig. 20** $^{13}$C NMR spectrum of tCzphB-Ph in $CDCl_3$.

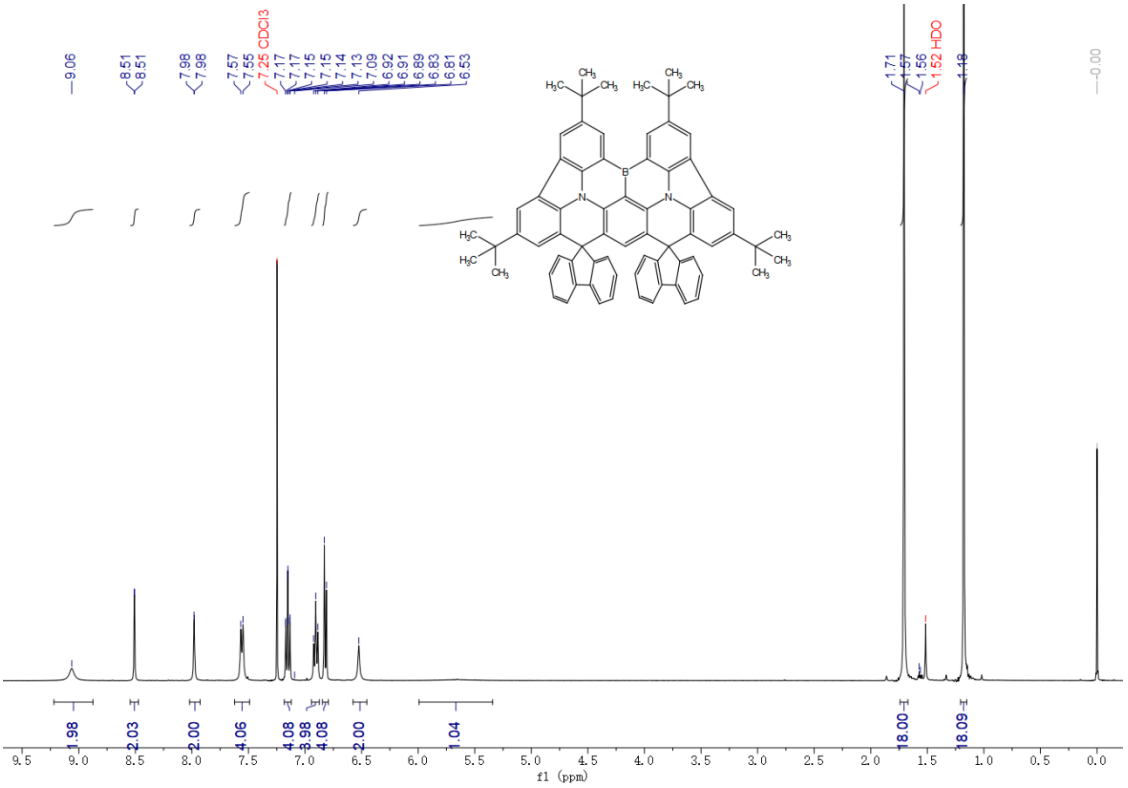


**Supplementary Fig. 21** $^{1}$H NMR spectrum of tCzphB-Fl in $CDCl_3$.

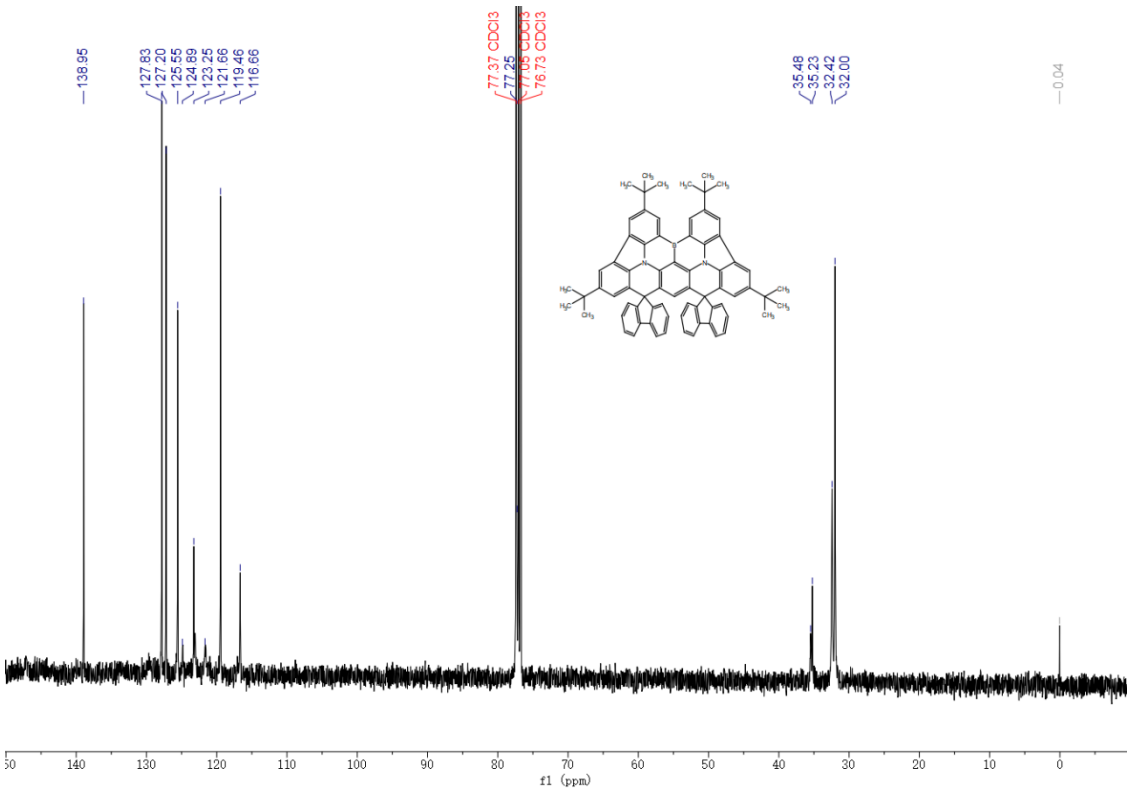


**Supplementary Fig. 22** $^{13}C$ NMR spectrum of tCzphB-Fl in $CDCl_3$.

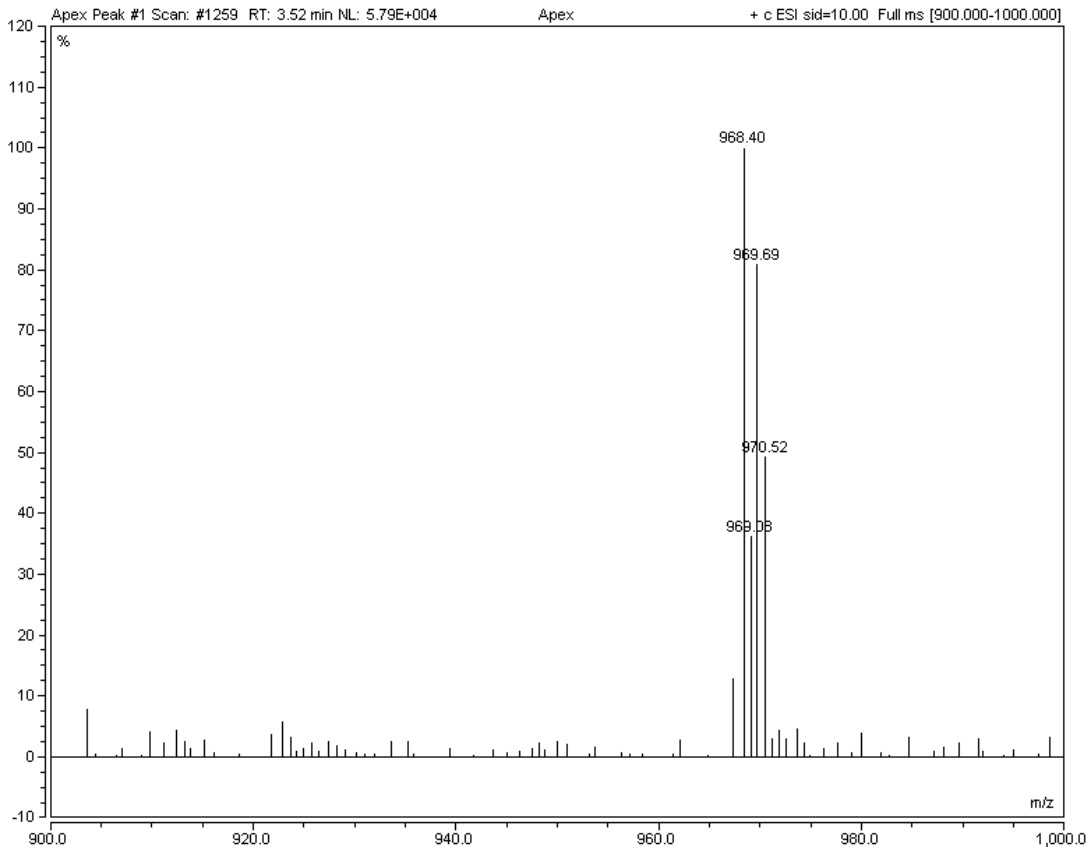


**Supplementary Fig. 23** ESI-MS spectrum of tCzphB-Ph, ESI-MS (M): m/z: 968.52 $[M]^+$ (calcd: 968.40).

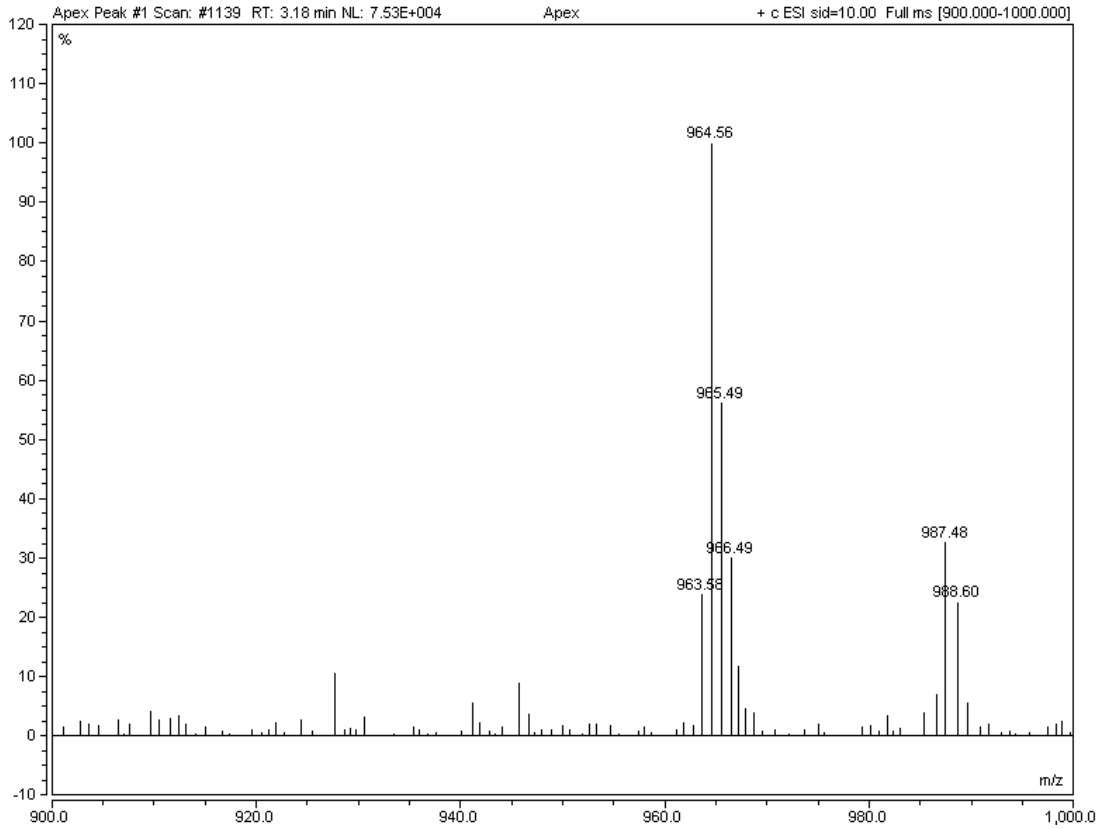


**Supplementary Fig. 24** ESI-MS spectrum of tCzphB-Fl, ESI-MS (M): m/z: 964.56 $[M]^+$ (calcd: 964.49), 987.48 for $[M+Na]^+$.

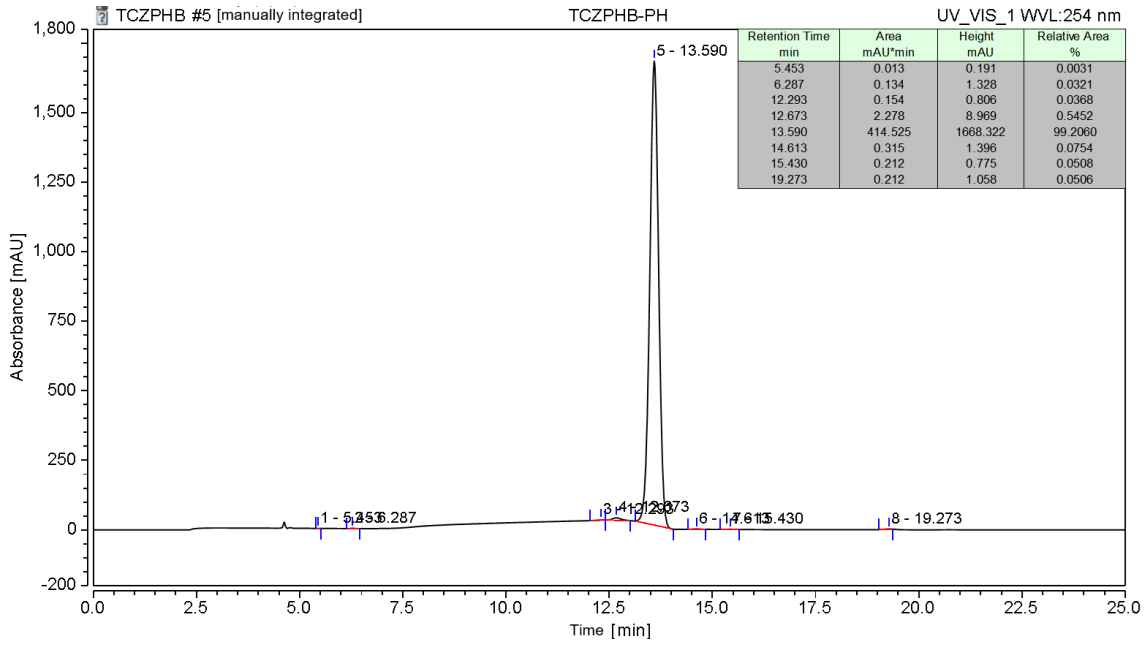


**Supplementary Fig. 25** High performance liquid chromatography (HPLC) spectrum of tCzphB-Ph (eluent: 25% THF/MeOH). The HPLC purity is 99.3%.

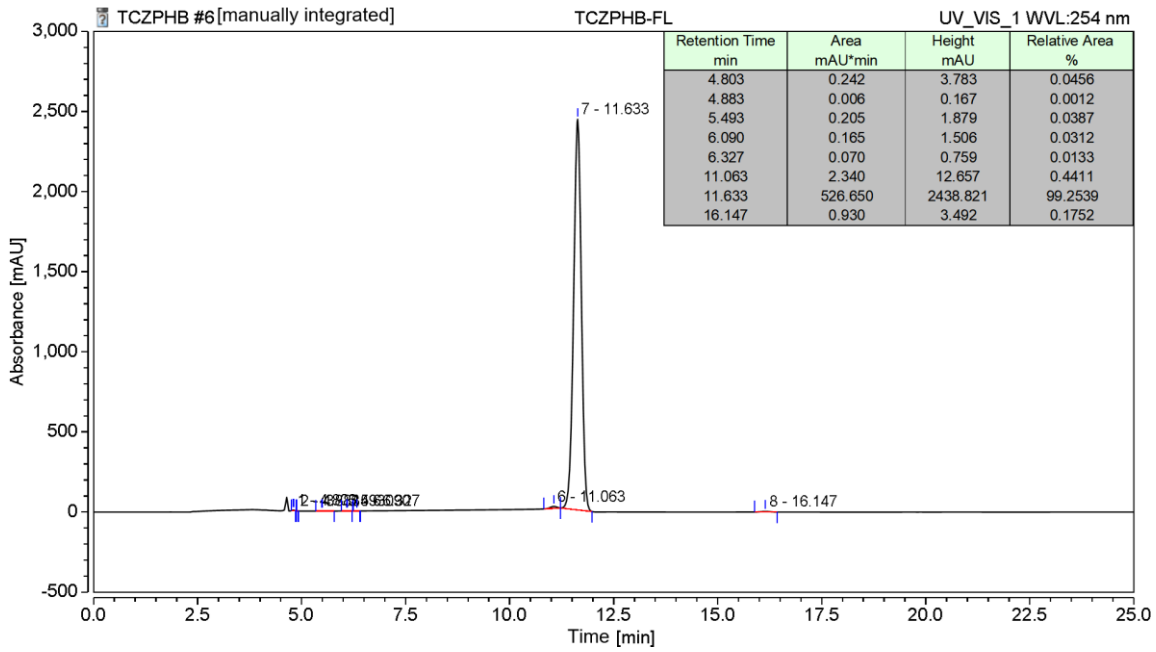


**Supplementary Fig. 26** High performance liquid chromatography (HPLC) spectrum of tCzphB-Fl (eluent: 25% THF/MeOH). The HPLC purity is 99.3%

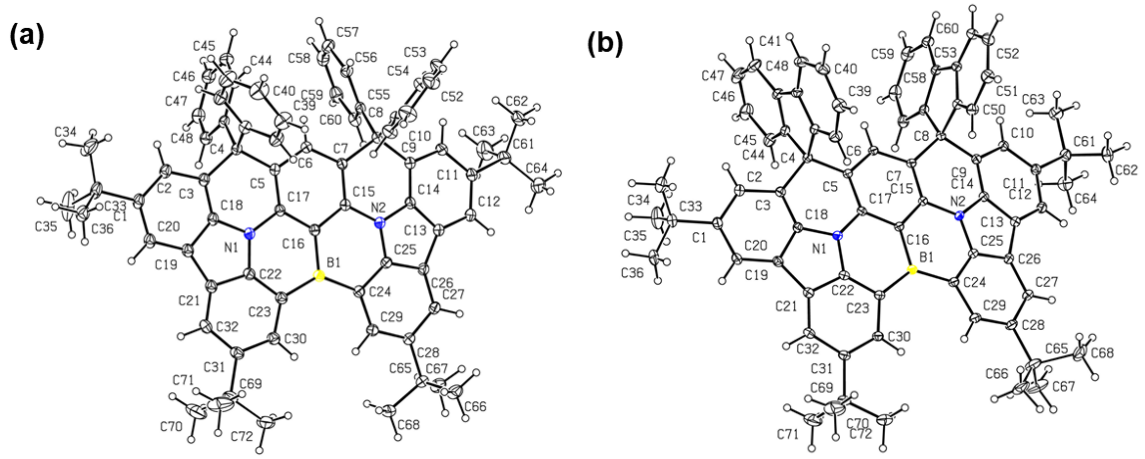


**Supplementary Fig. 27** ORTEP diagram of tCzphB-Ph **(a)** and tCzphB-Fl **(b)**.

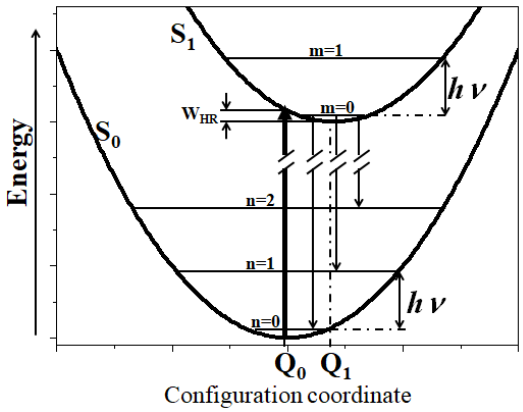


**Supplementary Fig. 28** Configuration coordinate (CC) diagram of the $S_1$ and $S_0$ electronic states with vibrational states, together with the electronic transitions. The potential energy parabolae are assumed to the same harmonic oscillations with energy $h\nu$. Coordinate $Q_0$ and $Q_1$ are equilibrium coordinates of the $S_1$ and $S_0$ states, respectively. $W_{HR}=k\Delta^2/2\equiv S\hbar\omega$, where S is Huang-Rhys factor and $\Delta=Q_1-Q_0$.

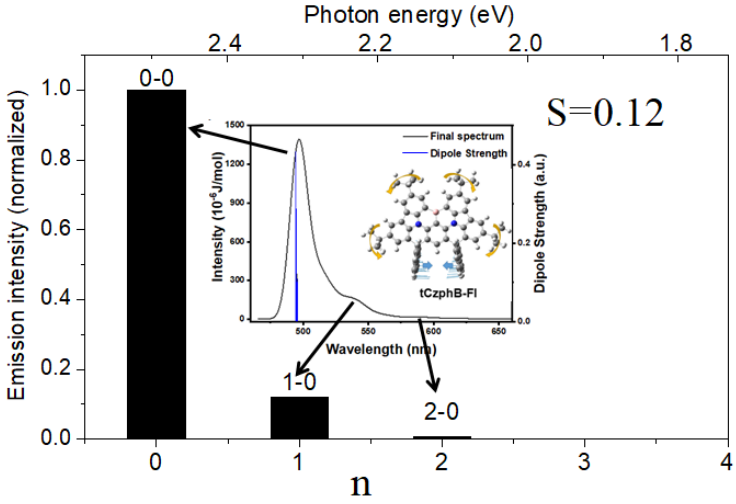


**Supplementary Fig. 29** Schematic profile of the relative intensities in the 0-0, 0-1, and 0-2 vibrational transitions of tCzphB-Fl under the Huang-Rhys factor S=0.12. Inset is the PL spectrum calculated by the TD-DFT method. The 0-3 and 0-4 transitions appear at n=3 and 4, respectively. They, however, are not shown because of too small intensities compared with the 0-2 transition. The upper photon energy scale is drawn to fit to the 0-0 peak energy (2.505 eV, ~495 nm) of the calculated PL spectrum with 0-1 peak energy (2.300 eV, ~539 nm), which gives the vibrational energy $h\nu_g$ (~0.20 eV, where $h$ is Planck's constant and $\nu_g$ is vibrational frequency) of the $S_1$ state. This corresponds to $\Delta n$=0.20 eV in the lower scale for integer n.

**Supplementary Table 1** Summary of Franck-Condon analysis on the $S_1$–$S_0$ transition of *t*-DABNA, DtBuCzB, tCzphB-Ph, and tCzphB-Fl at the (TD) PBE1PBE/6-31G(d,p) level.

| Compound | Transition ($S_1 \rightarrow S_0$) | frequency ($cm^{-1}$) | Relative frequency ($cm^{-1}$) | line density | dipole strength (arb. units) |
|---|---|---|---|---|---|
| *t*-DABNA | $0\rightarrow0$ | 23749.42 | 0 | 32.32 | 0.03318 |
| | $0\rightarrow1^1$ | 23736.49 | -12.9215 | 88.49 | 0.09105 |
| | $0\rightarrow1^2$ | 23723.57 | -25.843 | 126.7 | 0.1307 |
| | $0\rightarrow1^3$ | 23710.65 | -38.7645 | 126.3 | 0.1305 |
| | $0\rightarrow1^4$ | 23697.73 | -51.686 | 98.18 | 0.1017 |
| | $0\rightarrow1^5$ | 23684.81 | -64.6075 | 63.38 | 0.06581 |
| | $0\rightarrow12^11$ | 23664.63 | -84.791 | 37.73 | 0.03929 |
| | $0\rightarrow12^11^2$ | 23651.7 | -97.7125 | 51.78 | 0.05406 |
| | $0\rightarrow12^11^3$ | 23638.78 | -110.634 | 49.5 | 0.05177 |
| | $0\rightarrow12^11^4$ | 23625.86 | -123.556 | 36.93 | 0.03872 |
| DtBuCzB | $0\rightarrow0$ | 22146.54 | 0 | 476.1 | 0.6463 |
| | $0\rightarrow2^1$ | 22128.19 | -18.3462 | 111.4 | 0.1518 |
| | $0\rightarrow3^1$ | 22116.38 | -30.1583 | 118.2 | 0.1613 |
| | $0\rightarrow9^1$ | 22088.95 | -57.5857 | 503.3 | 0.6907 |
| | $0\rightarrow9^12^1$ | 22070.6 | -75.9319 | 112.9 | 0.1554 |
| | $0\rightarrow9^13^1$ | 22058.79 | -87.744 | 127.7 | 0.1761 |
| | $0\rightarrow9^2$ | 22031.37 | -115.171 | 266.8 | 0.3699 |
| | $0\rightarrow9^22^1$ | 22013.02 | -133.518 | 57.25 | 0.07963 |
| | $0\rightarrow17^1$ | 22001.71 | -144.822 | 75.23 | 0.1049 |
| | $0\rightarrow9^23^1$ | 22001.21 | -145.33 | 69.05 | 0.09629 |
| | $0\rightarrow9^3$ | 21973.78 | -172.757 | 94.5 | 0.1324 |
| | $0\rightarrow17^19^1$ | 21944.13 | -202.408 | 78.91 | 0.1112 |
| tCzphB-Ph | $0\rightarrow0$ | 20226.11 | 0 | 222.3 | 0.4338 |
| | $0\rightarrow2^1$ | 20215.3 | -10.813 | 147.1 | 0.2878 |
| | $0\rightarrow2^2$ | 20204.49 | -21.626 | 62.88 | 0.1232 |
| | $0\rightarrow5^1$ | 20193.29 | -32.8237 | 51.18 | 0.1006 |
| | $0\rightarrow11^1$ | 20184.77 | -41.341 | 62.59 | 0.1232 |
| | $0\rightarrow12^1$ | 20177.41 | -48.7005 | 55.46 | 0.1093 |
| | $0\rightarrow11^12^1$ | 20173.96 | -52.1541 | 33.18 | 0.06544 |
| | $0\rightarrow12^12^1$ | 20166.6 | -59.5135 | 43.19 | 0.08531 |
| tCzphB-Fl | $0\rightarrow0$ | 20105.92 | 0 | 736.5 | 1.766 |
| | $0\rightarrow6^1$ | 20074.22 | -31.7039 | 317.1 | 0.7653 |
| | $0\rightarrow6^2$ | 20042.51 | -63.4078 | 68.25 | 0.1657 |
| | $0\rightarrow15^1$ | 20036.96 | -68.958 | 100.2 | 0.2437 |
| | $0\rightarrow15^16^1$ | 20005.26 | -100.6619 | 43.49 | 0.1064 |
| | $0\rightarrow31^1$ | 19922.87 | -183.054 | 57.06 | 0.1419 |
| | $0\rightarrow32^1$ | 19910.37 | -195.5531 | 31.22 | 0.07787 |
| | $0\rightarrow123^1$ | 19419.90 | -686.0244 | 39.27 | 0.1082 |
| | $0\rightarrow143^1$ | 19299.98 | -805.9399 | 24.27 | 0.06856 |

**Supplementary Table 2** Summary of the reported green-emitting OLEDs with high color purity.

| Type | Compound | $\lambda_{EL}$ [nm] | $FWHM_{EL}$ [nm] | $EQE_{max}$ [%] | $L_{max}$ [kcd/m$^2$] | $CIE_{EL}$ [x, y] | Ref. |
|---|---|---|---|---|---|---|---|
| Fluorescence | C-545T | 500 | 60 | N.A. | 12 | [0.31, 0.65] | [1] |
| | tPhBODIPY | 520 | 32 | 19.0 | N.A. | [0.26, 0.67] | [2] |
| Phosphorescence | PtN7N | 518 | 24 | 22 | 10 | [0.27, 0.67] | [3] |
| TADF | 4CzIPN | 507 | 80 | 22.3 | 20 | [0.29, 0.58] | [4] |
| | CzDBA | 528 | 75 | 37.8 | <100 | [0.31, 0.61] | [5] |
| MR-TADF | 2F-BN | 501 | 40 | 22 | N.A. | [0.16, 0.60] | [6] |
| | DtBuPhCzB | 508 | 33 | 25.5 | 38 | [0.20, 0.65] | [7] |
| | m-Cz-BNCz | 520 | 44 | 27.0 | 26 | [0.23, 0.69] | [8] |
| | BBCz-G | 519 | 50 | 31.8 | <20 | [0.23, 0.65] | [9] |
| | AZA-BN | 527 | 30 | 28.2 | 10 | [0.27, 0.69] | [10] |
| This work MR-TADF | tCzphB-Fl | 535 | 26 | 26.2 | 37 | [0.26, 0.72] | |
| | tCzphB-Ph | 527 | 24 | 29.3 | 32 | [0.21, 0.75] | |
| | tCzphB-Ph | 526 | 27 | 31.3 | 520 | [0.21, 0.74] | |

**Supplementary Table 3** Length and bond order of the selected bonds (Supplementary Fig. 16) in the tCzphBs in their ground and excited states.

| | | Bond length (Å) | | | | Laplacian bond order | | | |
|---|---|---|---|---|---|---|---|---|---|
| Bond number | | **3** | **4** | **9** | **10** | **3** | **4** | **9** | **10** |
| tCzphB-Ph | $S_0$ | 1.54414 | 1.55634 | 1.55634 | 1.54414 | 0.896 | 0.853 | 0.853 | 0.896 |
| | $S_1$ | 1.53835 | 1.54905 | 1.54905 | 1.53835 | 0.914 | 0.876 | 0.876 | 0.914 |
| tCzphB-Fl | $S_0$ | 1.53663 | 1.54623 | 1.54623 | 1.53663 | 0.906 | 0.874 | 0.874 | 0.906 |
| | $S_1$ | 1.52923 | 1.53839 | 1.53839 | 1.52923 | 0.930 | 0.898 | 0.898 | 0.930 |

Note: The lengths of bond **4** and **9** in tCzphB-Ph are larger than the normal length of a C−C $\delta$-bond (~1.54 Å).[11]

**Supplementary Table 4** Crystal data and structure refinement for tCzPhB-Ph.

| | |
|---|---|
| Empirical formula | $C_{72}H_{65}BN_2$ |
| Formula weight | 969.07 |
| Temperature/K | 170.0 |
| Crystal system | triclinic |
| Space group | P-1 |
| *a*/Å | 15.1926(6) |
| *b*/Å | 15.9860(7) |
| *c*/Å | 17.0622(7) |
| *α*/° | 64.4760(10) |
| *β*/° | 69.0720(10) |
| *γ*/° | 66.3730(10) |
| Volume/Å$^3$ | 3339.6(2) |
| Z | 2 |
| $\rho_{calc}$g/cm$^3$ | 0.964 |
| $\mu$/mm$^{-1}$ | 0.055 |
| F(000) | 1032.0 |
| Crystal size/mm$^3$ | 0.42 × 0.28 × 0.2 |
| Radiation | MoKα (λ = 0.71073) |
| 2Θ range for data collection/° | 4.474 to 61.844 |
| Index ranges | $-21 \le h \le 19$, $-23 \le k \le 23$, $-24 \le l \le 24$ |
| Reflections collected | 82715 |
| Independent reflections | 20672 [$R_{int}$ = 0.0394, $R_{sigma}$ = 0.0401] |
| Data/restraints/parameters | 20672/357/781 |
| Goodness-of-fit on $F^2$ | 1.037 |
| Final R indexes [I>=2σ (I)] | $R_1$ = 0.0606, $wR_2$ = 0.1601 |
| Final R indexes [all data] | $R_1$ = 0.0873, $wR_2$ = 0.1750 |
| Largest diff. peak/hole / e Å$^{-3}$ | 0.44/-0.34 |

**Supplementary Table 5** Crystal data and structure refinement for tCzPhB-Fl.

| | |
|---|---|
| Empirical formula | $C_{72}H_{61}BN_2$ |
| Formula weight | 965.03 |
| Temperature/K | 170.0 |
| Crystal system | monoclinic |
| Space group | $P2_1/c$ |
| *a*/Å | 16.2161(6) |
| *b*/Å | 31.9970(11) |
| *c*/Å | 12.2815(3) |
| *α*/° | 90 |
| *β*/° | 104.3510(10) |
| *γ*/° | 90 |
| Volume/Å$^3$ | 6173.6(3) |
| Z | 4 |
| $\rho_{calc}$g/cm$^3$ | 1.038 |
| $\mu$/mm$^{-1}$ | 0.059 |
| F(000) | 2048.0 |
| Crystal size/mm$^3$ | 0.32 × 0.23 × 0.2 |
| Radiation | MoKα (λ = 0.71073) |
| 2Θ range for data collection/° | 4.266 to 66.2 |
| Index ranges | $-24 \leq h \leq 24$, $-49 \leq k \leq 44$, $-15 \leq l \leq 18$ |
| Reflections collected | 119473 |
| Independent reflections | 20615 [$R_{int}$ = 0.0501, $R_{sigma}$ = 0.0420] |
| Data/restraints/parameters | 20615/204/775 |
| Goodness-of-fit on $F^2$ | 1.030 |
| Final R indexes [$I$>=2σ ($I$)] | $R_1$ = 0.0616, $wR_2$ = 0.1725 |
| Final R indexes [all data] | $R_1$ = 0.1005, $wR_2$ = 0.2054 |
| Largest diff. peak/hole / e Å$^{-3}$ | 0.50/-0.81 |

## Supplementary Note 1. |Appearance of Narrow Emission Bands.

Three peaks are found in the simulated PL spectra of tCzphB-Ph, tCzphB-Fl, and DtBuCzB. For example, tCzphB-FI shows three simulated PL peaks at 500 nm (20000 $cm^{-1}$), 540 nm (18500 $cm^{-1}$), and 590 nm (16900 $cm^{-1}$), with almost the same separation of about 1550 $cm^{-1}$ between the two neighboring components, where the lowest-energy component intensity is considerably small (Fig. 3d). The same was found in tCzphB-Ph (or DtBuCzB) that shows peaks at 20110 (or 22000), 18580 (20450), and 16900 (18900) $cm^{-1}$, with separation of about 1600 (or 1550) $cm^{-1}$ (Fig. 3c and Supplementary Fig. 7b). These spectra are not inconsistent with the observed PL spectra (Fig. 2). When we use a model of harmonic parabola potentials for the excited and ground states with the same force constants (Supplementary Fig. 28) and vibrational modes, the three peaks are attributable to the 0-0, 0-1, and 0-2 vibrational transition components (Supplementary Fig. 29). Since the intensity ratio of the 0-1 component to the 0-0 one ($I_{0\text{-}1}/I_{0\text{-}0}$) is given by the Huang-Rhys factor S, the S factors are obtained to be 0.12, 0.13, and 0.11 for tCzphB-FI, tCzphB-Ph, and DtBuCzB, respectively (Fig. 3 and Supplementary Fig. 7).

This model predicts that the 0-3 vibrational component intensity is 0.000288 times of the 0-0 component band for tCzphB-FI with S=0.12. This intensity is too weak to be found in the actual spectrum measurement as the 0-2 component (Fig. 2). Unlike tCzphB-Ph, $Alq_3$ exhibits large Huang-Rhys factor of S~2.6, from which $Alq_3$ never shows a clear vibrational structure at RT. If such a large S factor would be obtained for tCzphB-Ph, this molecule would have never shown the narrow EL band. In this way we understand that small Huang-Rhys factor is responsible to the PL/EL band narrowing.

The Huang-Rhys factor S is given by $S\hbar\omega=k\Delta^2/2$, with force constant $k$ ($=M\omega^2$), where M is effective mass of molecule. A small S value is obtained by small potential shift $\Delta$ ($= Q_1-Q_0$) of the equilibrium coordinate $Q_1$ of the $S_1$ state from the equilibrium coordinate $Q_0$ of the $S_0$ state.[12] Supplementary Fig. 28 is drawn using the Franck-Condon (FC) factor $F_{n0}$ that is related with the coupling between the different vibrational states. In the present case of the transition from the vibrational 0 state of the excited state to the n (=0, 1, 2, 3…) vibrational states of the ground state, the FC factor is given by

$F_{n0}=e^{-S}S^n/n!$.[11] The small $Q_1$-$Q_0$ separation $\Delta$ due to small electron-phonon coupling is better to obtain narrow band spectrum by the following two reasons. The first is that the whole spectrum is predominantly determined by the 0-0 component and the contribution of the neighboring 0-1 component is nearly negligible. The relation of $I_{0\text{-}1}/I_{0\text{-}0}$=S indicates that a small 0-1 component intensity lead to a small S. The second is that the 0-1 component is located far from the 0-0 component which is located at $h\nu$ (or $\hbar\omega$) from the 0-0 component (Supplementary Fig. 28), since $\hbar\omega$ increases with decrease of S from the relation of $S\hbar\omega=k\Delta^2/2$, *i.e.*, $\hbar\omega=k\Delta^2/2S$. In summary, the contribution of the neighboring 0-1 component to the whole band width can be negligible because of the small Huang-Rhys factor S of 0.13.

Such a small S value is possible for the multi-resonance structured molecules like tCzphB-Ph with rigid chemical structure. Small S is generated by small $\Delta$, *i.e.*, small shift of the equilibrium position of the $S_1$ state from that of the ground state. One of the reasons for small shift is the rigidness which does not allow a large lattice relaxation after excitation into the excited state. The detailed analysis with evidence is under consideration.

It is noted that the simulated PL spectrum of tCzphB-Ph (Fig. 3d) consists of a lot of vibrational components (more than 850 components) due to various vibrational modes. For example, eight components are contained in a limited 60 $cm^{-1}$ range of 20226.11−20166.6 $cm^{-1}$ (Supplementary Table 1), which are caused by the modes-2, 5, 11, and 12 due to the rocking, twisting (rotation of *t*Bu-group), twisting (rotation of spiro-carbons with two phenyl groups), and scissoring (for whole molecule) vibrations, respectively, with different dipole strengths. These modes do not induce a vibration due to movements of atoms in boranaphtho[3,2,1-de]anthracene with one boron and two nitrogen atoms, suggesting a contribution to suppress the electron-phonon coupling in the $S_1 \rightarrow S_0$ transition.

## Supplementary Note 2. | Emission Band Narrowing in the cHex Solvent

Molecule tCzphB-Ph shows a PL spectrum with FHWM of 21 nm when it is dissolved in toluene (Fig. 2b), while a wider FWHM by 9 nm is observed in the CBP film doped with 2 wt% tCzphB-Ph (Fig. 2c). The PL band of tCzphB-Ph molecule exhibits a red shift when solvent is changed from cHex to toluene to THF to DCM, together with broadening of FWHM (Fig. 2c), *e.g.*, FWHM=14 nm in cHex solvent. Considerably narrow FWHM is obtained from tCzphB-Ph. The solvatochromism of the emission band peak shift, which follows the *Lippert-Mataga equation,* is based on the dipole-dipole coupling between the dipole moment of the emitter molecule and the dipole moment of the host molecule. A wider PL band with FWHM of 21 nm is observed in toluene compared with FWHM of 14 nm in cHex. This is due to the $\mu_G$=0.31 D and $\varepsilon_r$=2.38 for toluene, which are larger than the $\mu_G\approx$0 D and $\varepsilon_r$=2.02 for cHex, where $\mu_G$ and $\varepsilon_r$ are the dipole moment in the ground state and relative dielectric constant, respectively.

Larger dipole-dipole interaction between the tCzphB-Ph molecule and toluene solvent induces larger $\Delta$ shift because of reorientation of dipole moment of toluene molecules surrounding tCzphB-Ph molecule, compared with the non-polar cHex molecule. As a result, toluene gives rise to a larger S value than cHex. Consequently, unlike in cHex, the contribution of the 0-1 component to the broadening of the whole emission spectrum is negligible in toluene solvent. The closer location of the 0-1 component to the 0-0 component also contributes to the broadening since the distance $\hbar\omega$ between the two components becomes small and leads to spectral overlap, which is caused by smaller S from the above-mentioned relation $\hbar\omega=k\Delta^2/2S$. In this way the small FWHM of 14 nm observed in cHex than FWHM of 21 nm in toluene is understood.

## Supplementary Note 3. |Appearance of Long TADF Lifetime

According to the Fermi's golden rule, the reversed intersystem crossing rate between the initial ($T_1$) and final ($S_1$) states is expressed by

$$k_{RISC}=(2\pi/\hbar)<\varphi_{S1}(r)\chi_{S1,n}(Q)|H_{SO}(r)H_{vib}(Q)|\varphi_{T1}(r)\ \chi_{T1,n}(Q)>^2\rho(E_{S1})$$

$$k_{RISC}=(2\pi/\hbar)<\varphi_{S1}(r)|H_{SO}(r)|\varphi_{T1}(r)>^2\rho_{FCWD}$$

where $H_{SO}(r)$ and $H_{vib}(Q)$ are the spin-orbit and electron-phonon interaction Hamiltonians, respectively, while $\varphi_{S1}(r)$ and $\chi_{S1,n}(Q)$ are the electronic wavefunction of the $S_1$ state and the vibrational wavefunction of the *n*-th vibrational state in $S_1$, respectively. $\rho(E_{S1})$ is the density of the final $S_1$ state, and $\rho_{FCWD}$ is the Frank-Condon-weighted density of states that is derived from the Franck-Condon factor $<\chi_{S1,n}(Q)|\ \chi_{T1,n}(Q)>^2$. The Marcus-Levich-Jortner Theory based on the Franck-Condon Principle provides the following formula for $\rho_{FCWD}$:[13]

$$\rho_{FCWD} = \frac{1}{\sqrt{4\pi\lambda_M k_B T}} \sum_{n=0}^{\infty} \exp(-|S_{eff}) \frac{S_{eff}^n}{n!} \exp\left(-\frac{(\Delta E_{ST} + n\hbar\omega_{eff} + \lambda_M)^2}{4\lambda_M k_B T}\right)$$

where $S_{eff}$ is the effective Huang-Rhys factor of the effective mode with effective frequency $\omega_{eff}$, which is responsible to the strength of the electron-phonon coupling, and $\lambda_M$ is the reorganization energy, *i.e.*, the energy required to bring the system in the $S_1$ to the minimum structure of the $T_1$ state. The theory takes into account the overlap of the vibrational state between the $S_1$ state with vibrational state $n=n'$ and the $T_1$ state with $n=n''$ where the two states have the same energy, allowing the electronic reverse intersystem crossing transition from the $T_1$ state to the $S_1$ state. The part $\exp(S_{eff})n!/S^n_{eff}$ (defined as $C(S_{eff})$) involved the Huang-Rhys factor $S_{eff}$ gives a large value if $S_{eff}$ is small. Both tCzphB-Ph and tCzphB-FI give $S_{eff} \approx 0.12$ (Fig. 2d and Supplementary Fig. 7), and then gives the intensity for the 0-0 component ($n$=0), $C(S_{eff}=0.12) \approx 0.135$. Classical charge transfer (CT) molecules have a large $S_{eff}$ and a large $C(S_{eff})$ as a result, *e.g.*, $S_{eff}$=2.0 and $C(S_{eff}=2) \approx 14.8$.

Becasue $k_{RISC}$ is proportional to $k_{TADF}$, the delayed fluorescence lifetime $\tau_{TADF}$ is proportional to $\exp(-S_{eff})S^n_{eff}/n!$. Consequently, the two tCzphB-Ph and tCzphB-FI compounds are suggested to have much longer $\tau_{TADF}$, about by 109.6 (=14.8/0.135) times longer than the classical CT-type molecules. In this way, we understand the reason why

the present compounds exhibit long $\tau_{TADF}$ from the component related with the Huang-Rhys factor in the equation for $\rho_{FCWD}$ constructed by the Marcus–Levich–Jortner theory.

## Supplementary Note 4. |Synthesis of MR-TADF Emitters.

**Synthesis of 9,9'-(4,6-dibromo-1,3-phenylene)bis(3,6-di-tert-butyl-9H-carbazole)** (**A**):

60 mL anhydrous DMF was added into a 200 ml Schlenk flask, which contained 3,6-di-*tert*-butyl-9H-carbazole (11.3 g, 40.5 mmol), 1,5-dibromo-2,4-difluorobenzene (5.0 g, 18.4 mmol) and Caesium carbonate (18.0 g, 55.2 mmol), under a nitrogen atmosphere. The solution was refluxed with magnetic stirring for 24 h and then cooled down. The resulted solution was slowly poured into ice water (1 L) with stirring with glass rod. The powder solid was filtered out and dried in vacuum, and then further purified by column chromatography with a mixture eluent of ethyl acetate/petroleum ether (1:10), resulting in a white solid (**A**) of 13.2 g. Yield: 91 %. $^1$H NMR (400 MHz, chloroform-d) δ 8.36 (s, 1H), 8.11 (d, *J* = 1.8 Hz, 4H), 7.54 (s, 1H), 7.46 (dd, *J* = 8.6, 1.9 Hz, 4H), 7.08 (d, *J* = 8.6 Hz, 4H), 1.44 (s, 36H).

**Synthesis of 3,6,12,15-tetra-*tert*-butyl-8,8,10,10-tetraphenyl-8,10-dihydroindolo [1,2,3-*fg*]indolo [3',2',1':8,1]quinolino[3,2-*b*]acridine (B1):**

A solution of *n*-butyllithium in *n*-hexane (4.7 mL, 2.5 M, 11.7 mmol) was slowly added dropwise into a solution of compound **A** (4.0 g, 5.1 mmol) in anhydrous tetrahydrofuran (THF) (100 mL) at -78 ℃ under a nitrogen atmosphere. After stirring at -78 ℃ for 2 h, a solution of benzophenone (2.3 g, 12.7 mmol) in anhydrous THF was slowly added under a nitrogen atmosphere. Then the reaction mixture was slowly warmed to RT and stirred overnight. 20 mL diluted HCl solution (1 M), 400 mL distilled water and 150 mL ethyl acetate was added into the reaction mixture. The aqueous layer was separated and extracted with ethyl acetate three time (100 mL). The combined organic layers were dried with sodium sulphate, filtered. After removal of solvent under reduced pressure, the crude product was dissolved in anhydrous DCM (100 mL), and then 47% Boron trifluoride-diethyl etherate (2 mL) was added slowly at RT. The reaction mixture was stirred overnight, and slowly quenched by 100 mL $NaHCO_3$ aqueous solution, and then aqueous layer was separated and extracted with DCM (50 mL). The combined organic layers were dried with sodium sulphate, filtered, and concentrated by rotary evaporation. The product was further purified by column chromatography with using a

mixture eluent of DCM/petroleum ether (1: 20), afforded **B1** as a white solid (3.0 g, 61%). $^1$H NMR (400 MHz, chloroform-d) δ 8.67 (s, 1H), 8.24–8.04 (m, 4H), 7.93 (d, *J* = 1.7 Hz, 2H), 7.70 (dd, *J* = 8.7, 2.0 Hz, 2H), 7.15–7.06 (m, 14H), 7.01–6.87 (m, 8H), 6.75 (s, 1H), 1.51 (s, 18H), 1.34 (s, 18H).

**Synthesis of 3',6',12',15'-tetra-*tert*-butyldispiro[fluorene-9,8'-indolo[1,2,3-*fg*]indolo [3',2',1':8,1]quinolino[3,2-*b*]acridine-10',9''-fluorene] (B2)**

A similar procedure like synthesizing **B1** was carried out except replacing benzophenone with flourenone (2.3 g, 12.7 mmol), resulting in a white solid (3.2 g, 65 %). $^1$H NMR (400 MHz, chloroform-d) δ 8.78 (s, 1H), 8.35 (d, *J* = 8.7 Hz, 2H), 8.20 (d, *J* = 2.0 Hz, 2H), 7.92–7.78 (m, 4H), 7.55 (d, *J* = 7.6 Hz, 4H), 7.20 (td, *J* = 7.3, 1.3 Hz, 4H), 6.99–6.83 (m, 8H), 6.50 (d, *J* = 1.6 Hz, 2H), 5.65 (s, 1H), 1.57 (s, 18H), 1.15 (s, 18H).

**Synthesis of 19-bromo-3,6,12,15-tetra-*tert*-butyl-8,8,10,10-tetraphenyl-8,10-dihydroindolo[1,2,3-*fg*]indolo[3',2',1':8,1]quinolino[3,2-*b*]acridine (C1):**

After the chloroform solution (50 mL) of **B1** (2.0 g, 2.1 mmol) was cooled to 0 ℃ with strict exclusion of light, *N*-bromosuccinimide (NBS) (0.44 g, 2.5 mmol) was added stepwise into it. The reaction was maintained at 0 ℃ for 30 min and the stirring continued overnight at RT. The reaction mixture was poured into water (300 mL) and extracted with DCM, and the combined organic layers were dried with sodium sulphate, filtered, and concentrated by rotary evaporation. The product was further purified by column chromatography with using a mixture eluent of DCM/petroleum ether (1: 20), afforded **C1** as a yellowish solid (2.1 g, 97%). The obtained product was directly subjected to the next step without further purification.

**Synthesis of 19'-bromo-3',6',12',15'-tetra-*tert*-butyldispiro[fluorene-9,8'-indolo [1,2,3-*fg*]indolo[3',2',1':8,1]quinolino[3,2-*b*]acridine-10',9''-fluorene] (C2):**

A similar procedure like synthesizing **C1** was carried out except replacing **B1** with **B2** (2.0 g, 2.1 mmol), resulting in a yellowish solid (2.1 g, 95%). The obtained product was directly subjected to the next step without further purification.

**Synthesis of tCzphB-Ph:**

A solution of *n*-butyllithium in *n*-hexane (1.1 mL, 2.5 M, 2.8 mmol) was slowly added dropwise into a solution of compound **C1** (2.0 g, 1.9 mmol) in anhydrous tert-butylbenzene (80 mL) at -78 ℃ under a nitrogen atmosphere. When the addition was finished, the reaction mixture was slowly warmed to -40 ℃ and stirred at -40 ℃ for 2 h. After boron tribromide (0.5 mL, 5.6 mmol) has been added at -78 ℃, the reaction mixture was slowly warmed to RT and stirred overnight. *N*,*N*-diisopropylethylamine (0.8 mL, 5.6 mmol) was added at 0 ℃ and then the reaction mixture was stirring at 130 ℃ for 4 h. The reaction mixture was cooled to RT and quenched with 2 mL methanol. The reaction mixture was poured into water (300 mL) and extracted with DCM, and the combined organic layers were dried with sodium sulphate, filtered, and concentrated by rotary evaporation. The product was further purified by column chromatography with using a mixture eluent of DCM/petroleum ether (1:20), then recrystallized using DCM/methanol, afforded **tCzphB-Ph** as a yellow solid. (1.1 g, 61%). ESI-MS (M): m/z: 968.40 $[M]^+$ (calcd: 968.52). Anal. Calcd for $C_{72}H_{65}BN_2$: C, 89.23; H, 6.76; B, 1.12; N, 2.89. Found: C, 89.36; H, 6.77; N, 2.48. (B is not analyzed by elemental analysis). $^1$H NMR (500 MHz, methylene chloride-$d_2$) δ 8.92 (d, *J* = 1.7 Hz, 2H), 8.45 (d, *J* = 1.6 Hz, 2H), 8.01 (d, *J* = 1.4 Hz, 2H), 7.36 (s, 1H), 7.20 (d, *J* = 1.4 Hz, 2H), 7.11 – 7.03 (m, 20H), 1.58 (s, 18H), 1.27 (s, 18H). $^{13}$C NMR (101 MHz, chloroform-d) δ 130.04, 129.84, 127.94, 127.85, 127.71, 126.09, 125.99, 122.85, 116.35, 77.21, 35.33, 35.28, 32.39, 31.93.

**Synthesis of tCzphB-Fl:**

A similar procedure like synthesizing **tCzphB-Ph** was carried out except replacing **C1** with **C2** (2.0 g, 1.9 mmol), resulting in a yellow solid (0.9 g, 55 %). ESI-MS (M): m/z: 964.56 $[M]^+$ (calcd: 964.49). Anal. Calcd for $C_{72}H_{61}BN_2$: C, 89.61; H, 6.37; B, 1.12; N, 2.90. Found: C, 89.67; H, 6.47; N, 2.67. (B is not analyzed by elemental analysis). $^1$H NMR (400 MHz, chloroform-d) δ 9.06 (s, 2H), 8.51 (d, *J* = 1.5 Hz, 2H), 8.05–7.84 (m, 2H), 7.56 (d, *J* = 7.7 Hz, 4H), 7.15 (td, *J* = 7.5, 1.2 Hz, 4H), 6.91 (t, *J* = 7.4 Hz, 4H), 6.82 (d, *J* = 7.5 Hz, 4H), 6.53 (s, 2H), 5.65 (s, 1H), 1.71 (s, 18H), 1.18 (s, 18H). $^{13}$C NMR (101 MHz, chloroform-d) δ 138.95, 127.83, 127.20, 125.55, 124.89, 123.25, 119.46, 116.66,

77.25, 35.48, 35.23, 32.42, 32.00.

## Supplementary References


1. Lee, M.-T. *et al.* Efficient green coumarin dopants for organic light-emitting devices. *Org. Lett.* **6**, 1241–1244 (2004).
2. Song, X., Zhang, D., Zhang, Y., Lu, Y. & Duan, L. Strategically modulating carriers and excitons for efficient and stable ultrapure-green fluorescent OLEDs with a sterically hindered BODIPY dopant. *Adv. Opt. Mater.* **8**, 2000483 (2020).
3. Fukagawa, H., Oono, T., Iwasaki, Y., Hatakeyama, T. & Shimizu, T. High-efficiency ultrapure green organic light-emitting diodes. *Mater. Chem. Front.* **2**, 704–709 (2018).
4. Uoyama, H., Goushi, K., Shizu, K., Nomura, H. & Adachi, C. Highly efficient organic light-emitting diodes from delayed fluorescence. *Nature* **492**, 234 (2012).
5. Wu, T.-L. *et al.* Diboron compound-based organic light-emitting diodes with high efficiency and reduced efficiency roll-off. *Nat. Photon.* **12**, 235–240 (2018).
6. Zhang, Y. *et al.* Multi-resonance induced thermally activated delayed fluorophores for narrowband green OLEDs. *Angew. Chem. Int. Ed.* **58**, 16912–16917 (2019).
7. Xu, Y. *et al.* Molecular-structure and device-configuration optimizations toward highly efficient green electroluminescence with narrowband emission and high color purity. *Adv. Opt. Mater.* **8**, 1902142 (2020).
8. Xu, Y. *et al.* Constructing charge-transfer excited states based on frontier molecular orbital engineering: Narrowband green electroluminescence with high color purity and efficiency. *Angew. Chem. Int. Ed.* **59**, 17442–17446 (2020).
9. Yang, M., Park, I. S. & Yasuda, T. Full-Color, narrowband, and high-efficiency

electroluminescence from boron and carbazole embedded polycyclic heteroaromatics. *J. Am. Chem. Soc.* **142**, 19468–19472 (2020).

10. Zhang, Y. *et al.* Achieving pure green electroluminescence with CIEy of 0.69 and EQE of 28.2% from an aza-fused multi-resonance emitter. *Angew. Chem. Int. Ed.* **59**, 17499–17503 (2020).
11. Ishigaki, Y., Shimajiri, T., Takeda, T., Katoono, R. & Suzuki, T. Longest C–C single bond among neutral hydrocarbons with a bond length beyond 1.8 Å. *Chem* **4**, 795–806 (2018)
12. Shi-Jie X. Huang-Rhys factor and its key role in the interpretation of some optical properties of solids. *Acta Phys. Sinica* **68**, 166301–11 (2019).
13. Heller, E. R. & Richardson, J. O. Semiclassical instanton formulation of Marcus–Levich–Jortner theory, *J. Chem. Phys.* **152**, 244117 (2020).